Extraordinary second harmonic generation modulated by divergent strain field in pressurized monolayer domes ⑤

Boqing Liu ⓘ ; Tanju Yildirim ⓘ ; Elena Blundo ⓘ ; Domenico de Ceglia ⓘ ; Ahmed Raza Khan ⓘ ;
Zongyou Yin ⓘ ; Hieu T. Nguyen ⓘ ; Giorgio Pettinari ⓘ ; Marco Felici ⓘ ; Antonio Polimeni ✉ ⓘ ;
Yuerui Lu ✉ ⓘ

Check for updates

View Online   Export Citation

Articles You May Be Interested In

Giant second harmonic generation in two-dimensional tellurene with synthesis and thickness engineering

Appl. Phys. Rev. (February 2025)

Optimal photonic nanojet beam shaping by mesoscale dielectric dome lens

J. Appl. Phys. (June 2020)

Strain engineering of the transition metal dichalcogenide chalcogen-alloy WSSe

J. Appl. Phys. (June 2024)

AIP Publishing

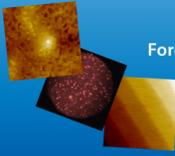# Extraordinary second harmonic generation modulated by divergent strain field in pressurized monolayer domes ⓕ

View Online　　Export Citation　　CrossMark

Boqing Liu,[1] ⓘ Tanju Yildirim,[2] ⓘ Elena Blundo,[3] ⓘ Domenico de Ceglia,[4] ⓘ Ahmed Raza Khan,[1] ⓘ
Zongyou Yin,[5] ⓘ Hieu T. Nguyen,[1] ⓘ Giorgio Pettinari,[6] ⓘ Marco Felici,[3] ⓘ Antonio Polimeni,[3,a] ⓘ
and Yuerui Lu[1,7,a] ⓘ

AFFILIATIONS

[1]School of Engineering, College of Engineering, Computing and Cybernetics, The Australian National University,
 Canberra ACT 2601, Australia
[2]Research Center for Macromolecules and Biomaterials, National Institute
 for Materials Science (NIMS), 1-1 Namiki, Tsukuba, Ibaraki 305-0044, Japan
[3]Dipartimento di Fisica, Sapienza Università di Roma, Roma 00185, Italy
[4]CNIT and Department of Information Engineering, University of Brescia, Brescia 25123, Italy
[5]Research School of Chemistry, College of Science, The Australian National University, Canberra ACT 2601, Australia
[6]Institute for Photonics and Nanotechnologies, National Research Council, 00133 Rome, Italy
[7]ARC Centre of Excellence in Quantum Computation and Communication Technology ANU Node, Canberra ACT 2601, Australia

[a]Authors to whom correspondence should be addressed: antonio.polimeni@uniroma1.it and yuerui.lu@anu.edu.au

ABSTRACT

The most prominent form of nonlinear optical (NLO) frequency conversion is second harmonic generation (SHG), where incident light interacts with a nonlinear medium producing photons at double the input frequency, which has vast applications in material and biomedical science. Emerging two-dimensional nonlinear optical materials led by transition metal dichalcogenides (TMDs) have fascinating optical and mechanical properties and are highly anticipated to overcome the technical limitations imposed by traditional bulky NLO materials. However, the atomic scale interaction length and low conversion efficiency in TMD materials prevent their further implementation in NLO applications. While some uniaxial strain-engineering studies intensively investigated the anisotropic SHG response in TMDs, they did not realize giant SHG enhancement by exploiting the opto-mechanical characteristics. Herein, we employ proton (H^+) irradiation to successfully fabricate large pressurized monolayer TMD domes ($d \geq 10\,\mu$m) and conduct a comprehensive investigation and characterization of their SHG performance enhancement. We show that the intensity of SHG is effectively enhanced by around two orders of magnitude at room temperature. Such giant enhancement arises from the distinct separation distance induced by capped pressurized gas and the hemi-spherical morphology, enabling constructive optical interference. Moreover, the unique divergent strain field in TMD domes promotes the first experimental study on the anisotropic nonlinear optical behavior based on biaxial strain conditions in terms of varying strain orientation and relative weights. Our work demonstrates a promising system with enhanced NLO performance and well-preserved biocompatibility, paving a way toward the future nano-scaled quantum optics design and biomedical applications.

INTRODUCTION

Materials with broken inversion symmetry possess a non-vanishing second-order nonlinear optical susceptibility, $\chi_0^{(2)}$. When these materials are exposed to an intense optical pump, they can give rise to strong second-harmonic generation (SHG), resulting in the frequency doubling of a light wave. Such a strong nonlinear frequency conversion process has paramount importance for applications, including light generation, quantum photonics, optical signal processing, and imaging.[1–5] Furthermore, SHG is frequently utilized to identify material properties, such as crystal symmetry, band structure,[6,7]

lattice orientation,[8,9] polar domains and magnetic ordering,[10] surfaces, and quantum interference.[11] On the other hand, due to the weak photon–photon interactions in traditional nonlinear optical (NLO) materials, the high SHG output heavily relies on large pumping power, bulky interaction volumes, and proper phase-matching conditions. This becomes the substantial challenge in miniaturized nonlinear optical devices for future applications. The emergence of two-dimensional nonlinear materials is anticipated to provide the solution for novel nonlinear optics to overcome the technical limit imposed by traditional NLO materials. One of the most outstanding candidates is transition metal dichalcogenides (TMD) of the form MX_2 (M = Mo, W and X = S, Se). As one transition metal atom is sandwiched between two layers of chalcogen atoms in each monolayer TMD crystal, broken inversion symmetry only exists in TMD crystals having an odd number of layers, which leads to a large second-order susceptibility $\chi_0^{(2)}$ and strong SHG intensities at the atomic thickness level.[12–15] In addition, TMD films also possess remarkable mechanical flexibility and robustness, enabling them to withstand large stretching and mechanical deformation,[16–19] and have great potential for flexible optical devices.

Currently, one of the primary barriers in the practical application of TMD materials' SHG capability is the atomically thin light–matter interaction length scale, resulting in low conversion efficiency. The common approaches for enhancing SHG intensity heavily rely upon external hardware setups including photonic crystal resonators[20–22] and external voltage modulation,[22,23] which have limited applicability due to tedious sample preparation and fabrication processes. In contrast, strain-engineering techniques can effectively manipulate optical properties and bring novel features,[24] including strain induced bandgap modulation,[25,26] exciton funneling effects,[16] and single photon emission.[27,28] While some work claimed heavy SHG emission quenching caused by applied strain,[29,30] a previous report using a wrinkling technique achieved moderate enhancement in SHG emssion,[31] meaning strain has adverse effects on SHG emission. At the same time, previous strain engineering approaches primarily focused on the anisotropic SH response under uniaxial strain,[24,30–33] instead of SHG enhancement. This condition appears to imply that traditional strain engineering fails to capitalize on the mechanical features of TMD materials and their resulting SHG performance.

In this work, we successfully fabricate pressurized monolayer TMD domes with radii up to a few micro-meters and conduct comprehensive SHG measurements. The hemi-spherical geometry of domes and large internal gas pressure effectively improve SHG emission with two orders of magnitude at room temperature and one order of magnitude enhancement at −190 °C, compared to the unstrained TMD monolayer flakes in the C exciton peak range. Moreover, taking advantage of enhanced SHG responses and unique diverging strain field in TMD domes, we first experimentally investigate and reveal the influence of biaxial strain on the anisotropic SHG response. The minor evolution of the lattice distortion caused by biaxial strain in various magnitudes and directions is clearly probed via polarization resolved SHG, and corresponding anisotropic responses are clearly depicted in SHG polar plots. According to our work, we believe TMD domes exhibiting extraordinary SHG emission will become promising candidates for future nonlinear optical devices and biomedical imaging and sensing devices.

RESULTS AND DISCUSSION
SHG mechanism in dome structures

In this work, the dome formation was achieved by the proton (H+) irradiation method. By being accelerated by an electric field, protons penetrate the top few layers of TMD flakes and subsequently reduce to hydrogen gas, trapped beneath the flake's uppermost few layers.[34] The competition between interlayer adhesion energy, elastic energy of the TMD film, and pressure of the capped gas reaches an equilibrium state, forming stable domes [Fig. 1(a)][35,36] that have a universal shape and endure for a very long time without any structural changes.[37,38] This method allows domes to range in sizes from a few to dozens of micrometers, making it possible to conduct SHG measurements on domes as well as other far field optical studies.[39,40] As TMD domes would serve as the local suspension, those with an odd number of layers would become the nonlinear optical emitters grown on the bulk flake [Fig. 1(b)]. By conducting SHG mapping measurements on the dome samples, we found that most domes are monolayer as they have strong SHG emission compared to the bulk flake.

For different dome sizes, the strongest emission zones are not consistently found at the center. This fact could be explained as optical interference occurred within the dome structure. When the fundamental light (near infrared light source λ) strikes on the dome surface, a portion of the fundamental light would interact with the TMD monolayer and convert into the backward SHG emission ($\lambda/2$) from the dome surface and forward SHG light emitted from the inner side of the TMD film. Simultaneously, the forward SHG and the remainder of fundamental light would impinge on the upper surface of bulk flake and get reflected, and then the reflected forward SHG would pass through the monolayer film while the reflected fundamental light will strike the film again and generate another forward SHG in the upward direction. During the process, if the height (h) between any site on the dome surface and the bottom can be converted to the path length difference equal to an odd multiple of $\lambda_{pump}/4$, all these SHG light waves would be in phase and undergo the constructive interference, generating a strong local emission [Fig. 1(c)]. In order to confirm this, AFM and SHG mapping measurements were performed on 3 individual domes which vary in size and intensity patterns [Fig. 1(d)]. Through extraction and comparison of the height and SHG intensity profiles of these domes, we found that these domes share a common aspect ratio ($h/R = 0.18$),[34] and the bright fringes can only exist when the domes' height exceeds around 160 nm. For the optical pattern of dome 1, the largest SHG is located at the center of the dome, as the height of dome 1 nears 160 nm. For those domes gradually larger than dome 1, the largest SHG emission area would transform from the central point to bright round fringes, with the relocation from the dome center to the location with separation heights of around 160 nm. The greatest SHG emission site would return to the center of the dome as the dome height increased, as was the case with dome 3 (whose height reached 260 nm). To determine the link between SHG intensity and dome height, the SHG intensity at the summit of many domes was extracted as shown in Fig. 1(e). It is clear to see that the SHG intensity would reach the maximum when the height is around 150 nm, then decline until the height was over 225 nm, at which point SHG intensity increased again. This was also the case for WS_2 domes (Fig. S1). This trend could be well described by an analytical solution based on a standing wave in the dome structure of the form
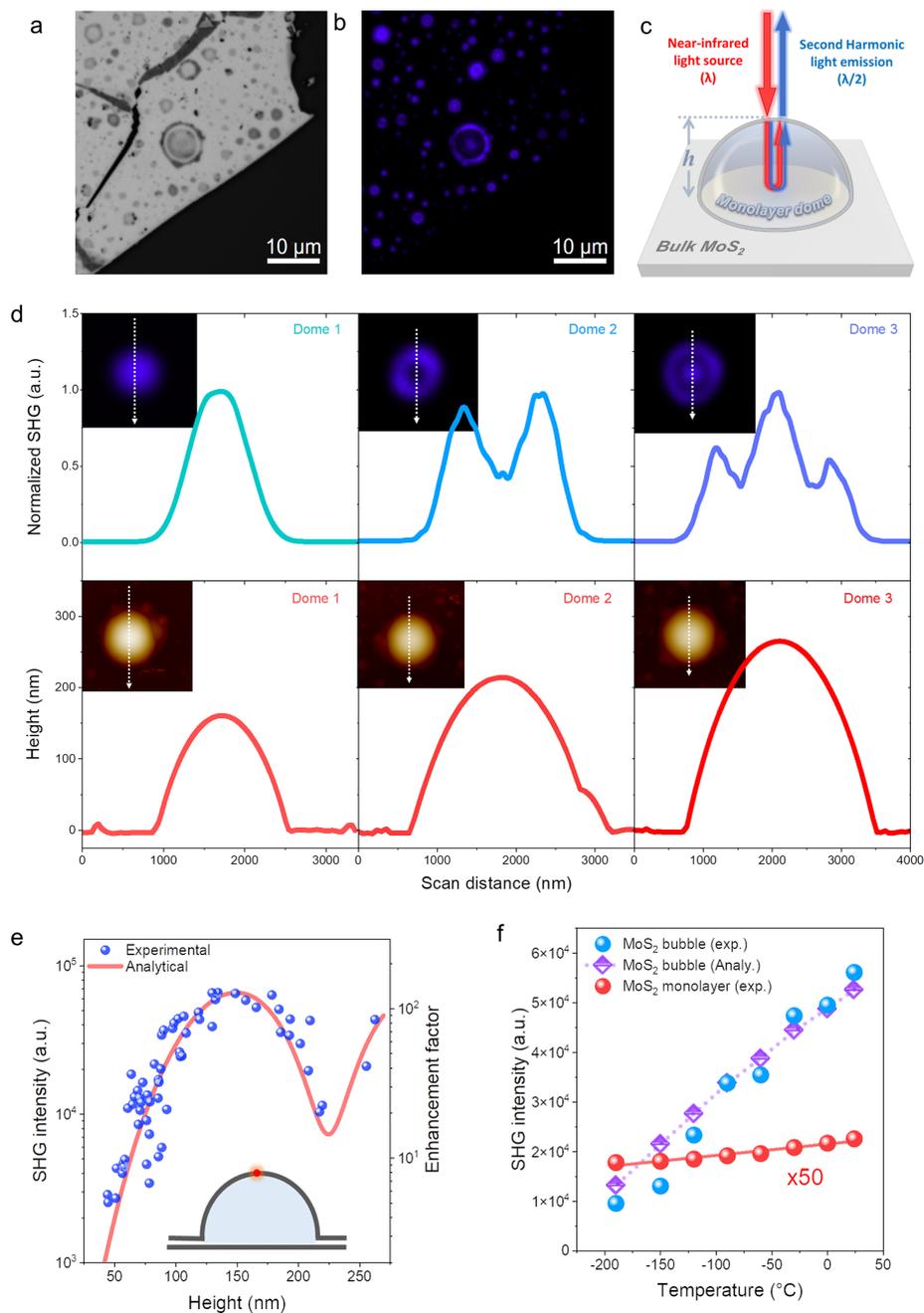
FIG. 1. Second harmonic optical response in MoS$_2$ pressurized domes. (a) Optical microscope image of pressurized domes formed on top of an MoS$_2$ flake. (b) Second harmonic generation (SHG) intensity mapping of the domes on the same flake shown in Fig. 1(a), the wavelength of the pump laser is 900 nm. Under the same excitation and collection conditions, monolayer (1L) domes exhibit the strongest SHG signal, whereas bilayer (2L) domes are invisible due to their centrosymmetric crystal orientation. (c) SHG mechanism in a ML dome. The red and blue wavy lines represent near infrared pump source and SHG output, respectively. (d) Extracted profile plots for different sized domes. Top panels display the normalized SHG intensity profile (purple) of the domes along the white dashed line of the SHG mapping image shown in the insets. Bottom panels: the measured height profile (red) of the corresponding domes along the white dashed line in insets obtained from atomic force microscope (AFM) images of each dome. (e) Experimental (blue spheres) SHG intensities collected at the top of domes (inset) as a function of dome's height. Analytical values (red line) match well with experimental results; right vertical axis: the enhancement factor of SHG compared with the 1L MoS$_2$ flake on SiO$_2$ (275 nm) substrate under the same excitation wavelength (900 nm) and power. (f) Temperature-dependent SHG measurements conducted on the 1L MoS$_2$ dome with 127 nm height (blue spheres) and the ML flake (red spheres), where the experimental SHG results obtained at different height induced by decreasing temperature have a good agreement with analytical SHG results in terms of dome height based on the RT condition (purple diamond).

$$I_{SH} \propto I_{pump} \cdot |(1 + \rho_p e^{j2k_p h})^2 \cdot (1 + \rho_{SH} e^{j4k_p h})|^2, \quad (1)$$

where h is the dome height, and $\rho_p = (1 - n_p)/(1 + n_p)$, $\rho_{SH} = (1 - n_{SH})/(1 + n_{SH})$ represent the reflection coefficient for the pump and SH lights, respectively, and n_p and n_{SH} are the refractive indices at pump and SH wavelengths, respectively. According to the analytical results, which shows great agreement with the numerical solution (Fig. S2), the SH intensity must have a strong dependence on the radial distance induced by the local height of the dome (separation distance), as this changes along the dome surface. Once the height of the dome reaches the critical value, the center would intermittently turn into the brightest emitter, accompanied by fringes as shown in Fig. 1(d). This is well supported by the patterns generated by the analytical method (Fig. S3), although there is minor discrepancy induced by the imaging resolution which cannot resolve more narrow fringes within the limited pixel lateral dimension. Thus, the optical pattern in Figs. 1(b) and 1(d) arises from constructive and destructive optical interference, which is also confirmed by the results of optical height obtained by phase shift interferometry (Fig. S4). Furthermore, even though the biaxial strain exerted on the dome samples would lead to a limited increase in the second order susceptibility $\chi^{(2)}$,[41] the constructive interference created by the local height of dome system is the dominant factor for the extraordinary SHG at the dome center, which enables 160 times enhancement compared to the monolayer MoS$_2$ flake on a 275 nm SiO$_2$ substrate. This enhancement factor is comparable to TMD monolayer flakes integrated into a photonic cavity device,[20] suggesting the great potential of TMD domes for future optical applications.

To further investigate the importance of the separation distance against total SH emission of the dome, temperature-dependent SHG measurements are carried out. When decreasing the environment temperature from room temperature (RT) to $-190\,^{\circ}$C, the SHG intensity of the dome declined by 83.4%, and this quenching factor was about 4 times larger than the value of a freestanding monolayer MoS$_2$ sample [21.1% shown in Fig. 1(f)]. This greater quenching factor is mainly due to the reduced dome volume (shrinking) because of the low temperature. The height of a dome is linearly proportional to temperature and decreased by $\sim$73% as the temperature dropped from RT to $-190\,^{\circ}$C. The same trend was also detected for WS$_2$ domes (Fig. S5). This proves that significant height variation would greatly affect phase matching for the constructive optical interference leading to exponential decay in total SH emission, in stark contrast to TMD monolayer flakes whose SHG intensity changes linearly with modifying lattice dimensions induced by thermal expansion.[42] Moreover, based on the assumption of a constant aspect ratio ($h/R = 0.18$) of domes with temperatures and the estimation of the dome height at different temperature, the comparison between the experimental result of temperature-dependent SHG and analytical results at corresponding height values exhibited a good consistency. This directly further proves that the separation distance in the dome system plays the dominant role in dramatic SH emission changes. It is worth noting that despite the substantial intensity fall for the SH emission in the dome at low temperatures, the absolute SH intensity of the dome is still significantly higher than that of the monolayer flake.

Such robust enhancement observed in TMD monolayer domes enable them to become high-conversion-efficiency light emitters, which may have profound implications for future nonlinear optical devices such as quantum photonics and optical parametric generation

(OPG).[43] Meanwhile, the large size and hemi-spherical geometry of domes can serve as a non-bleaching optical probe offering outstanding up and down conversion fluorescent capability,[44–46] demonstrating great potential for future biomedical diagnostic and imaging applications even in the extreme conditions.

Polarization-dependent SHG on biaxial strain

Polarization-dependent SHG is an effective technique to identify and resolve lattice distortion, as the strain would modulate the second-order nonlinear susceptibility tensor $\chi^{(2)}_{ijk}$ and break the symmetry in the SHG polarization pattern.[47] Pressurized TMD domes are a promising candidate for SHG studies, linking complex strain components to nonlinear optical properties. In addition to the enhanced intensity and predictable locations of SHG fringes brought on by the optical interference, the domes also have differing strain components in both magnitude and orientation directions that heavily influence SHG. Here, polarization-dependent SHG measurements were conducted at multiple locations to investigate the permanent biaxial strain in circumferential and radial directions (θ_h and θ_r) exerted on the pressurized TMD domes, where θ_r is equivalent to the azimuthal angle with respect to the center of the dome and is perpendicular to θ_h.

Since domes are formed by the competition between internal gas pressure, elastic energy, and van der Waals adhesion energy of the TMD film,[36,48] there is a divergent strain field over the dome surface. When moving away from the dome summit toward the edge, the biaxial strain is radially distributed and finally results in uniaxial strain from the center to the edge of the dome,[32,34,35] ranging from around 5% to 2% as determined by the methods in SI Note 1 and demonstrated in Fig. S6(a). The strain variation is further confirmed by the phonon mode shifts depicted in location-dependent Raman spectra (Fig. S7, supplementary material Note 2). To investigate the influence of the bi-axial strain magnitudes on the lattice distortion, multiple sites were examined from the top toward the bottom of the dome. For simplicity, like the coordinates on earth which can be described by latitude and longitude, test sites on the TMD dome can also be determined by the orientation of the radial strain component, θ_r, and the ratio of radial distance from dome center, r/R. Locations at $r/R = 0$, 0.16, 0.26, 0.32, and 0.39 in a certain radial direction ($\theta_r = 20\,^{\circ}$) were selected [Fig. S6(b)], whose decreasing trend of the total strain is also confirmed by blueshifts in PL and Raman spectra extracted at those corresponding locations [Figs. S8(a) and 8(b)]. The corresponding experimental SHG polar patterns under the application of various levels of biaxial strain are depicted in Figs. 2(a)–2(e). When the examined site was at the top of the dome, equal bi-axial strain components ($\varepsilon_r = \varepsilon_h$) exist, and the lattice would be stretched with the same displacement. The corresponding SHG polar pattern, thus, would remain the same shape as in unstrained flakes,[15,33,49] featuring six uniform petals [Fig. 2(a)]. However, with locations away from the top of the dome, the uneven biaxial strain leads to distorted patterns, and the size of petals, i.e., anisotropic SH response, is influenced and manipulated by the ratio between the two strain components [Figs. 2(b)–2(e)]. As the radial distance increases, the relative weight of ε_r on the total biaxial strain becomes greater; therefore, the overall pattern shape is reduced in θ_h and elongated in θ_r [Fig. 2(e)], indicating the differing in-plane displacement of Mo and S atoms sustained via different levels of strain components.[30]
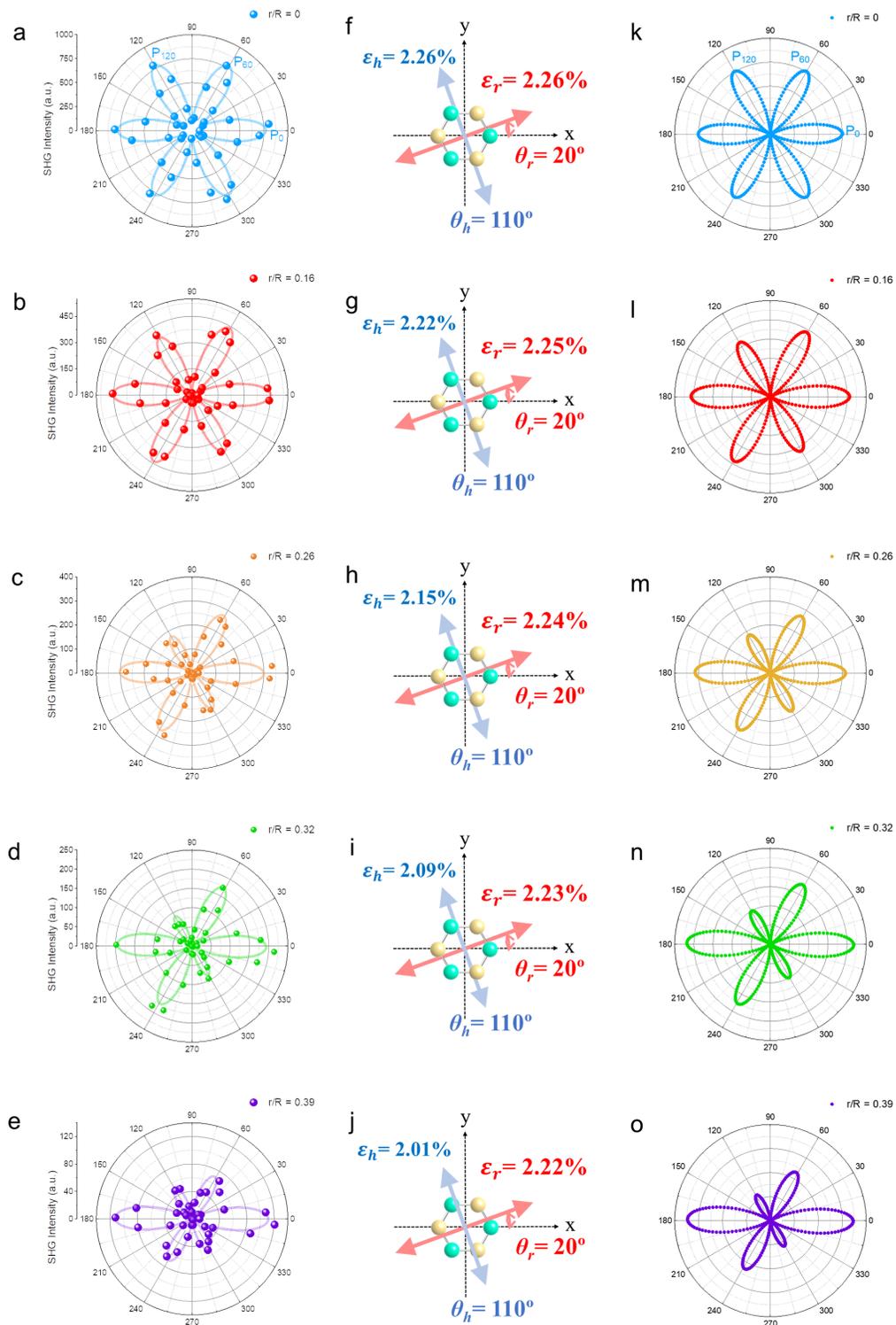
08 June 2025 23:52:08

FIG. 2. Probing the anisotropic SH response with the evolution of the lattice distortion induced by varying biaxial strain magnitudes. (a)–(e) Polarization-resolved SHG measured experimentally with varied levels of strain in the same θ_r (f)–(j) Schematic illustrations of the strain conditions at various sites distant from the dome's center from the top view, where the values of ε_r (red arrow) and ε_h (blue arrow) change with the radius in the same principal orientation of the radial strain, $\theta_r = 20°$. (k)–(o) Analytical results of polarization-resolved SHG at different sites with the corresponding strain magnitudes in the same direction as shown in (f)–(j), respectively.

To understand SHG polar pattern evolution and the involved photoelastic effect, an established approach was employed for the analytical SHG polar pattern evolution under strain. The parallel polarized SHG intensity "$I_{//}(2\omega)$" under bi-axial strain for D_{3h} symmetry class considering the photoelastic effect has the form[50]

$$I_{//}(2\omega) \propto \frac{1}{4}[A\cos(3\phi - 3\delta) + B\cos(2\theta_r + \phi - 3\delta)]^2, \quad (2)$$

where $A = (1-\nu)(p_1 + p_2)(\varepsilon_r + \varepsilon_h) + 2\chi_0^{(2)}$ and $B = (1+\nu)(p_1 - p_2)(\varepsilon_r - \varepsilon_h)$, p_1 and p_2 are the photoelastic coefficients, ν is Poisson's ratio, θ_r is radial strain direction, ϕ is the polarization angle, δ is the armchair direction and $\chi_0^{(2)}$ is the nonlinear susceptibility parameter of the unstrained crystal lattice. The strain conditions at the investigated sites were determined [Eqs. (S2) and (S3)] by taking advantage of the universal h/R ratio and the corresponding radial distances r/R of the sites (supplementary material Note 1). Hence, the strain conditions (ε_r, ε_h, and θ_r) at corresponding test sites, as indicated in Fig. S6(b), are interpreted as (2.26%, 2.26%, 20°), (2.25%, 2.22%, 20°), (2.4%, 2.15%, 20°), (2.23%, 2.09%, 20°), and (2.22%, 2.01%, 20°), respectively. According to these values, the analytical polar patterns were subsequently generated, and they displayed the same trend in lattice distortion as described in the evolution of the pattern shape with locations. The plots at the top of the dome have a uniform six-fold rotational symmetry, while plots with breaking symmetry induced by the lattice distortion were found in the other locations aside from the center [Figs. 2(k)–2(o)], which has a great agreement with the experimental data. Therefore, considering the strain ratios in specific orientations, larger petals correspond to the larger strain level and minimum angle difference between θ_r and armchair direction δ of the lattice, while the less strained direction would lead to shrunken petals. Unlike the case of uniaxial strain, the local lattice is not significantly distorted despite the large amount of total strain applied.[30,33,50]

Moreover, as the strain magnitudes are directly related to the coordinates on the dome surface, locations with the same radial distance away from the center of the dome are supposed to share the same strain magnitudes. To further monitor the lattice distortion in various directions, polarization-dependent measurements were conducted in a circumferential direction on the surface of the dome. For convenient positioning and measurement, the test sites were selected along a bright fringe circle of a monolayer dome sample. The armchair direction δ of the dome sample was initially aligned with the horizontal direction (x axis), so the orientations of ε_r are equivalent to the azimuthal angles of test sites as shown in Fig. S6(c), leading to multi-angular strain components with the same magnitude. In Figs. 3(a)–3(e), the SHG polar plots were experimentally obtained from test sites with azimuthal angles of 30°, 60°, 90°, 120°, and 150°. The distorted sixfold SHG patterns indicate that biaxial strain with uneven components exist at these sites, and each site withstood the same magnitude of total strain as indicated by the corresponding PL and Raman spectra in Figs. S8(c) and S8(d). In addition, the varying orientations of biaxial strain applied were clearly interpreted as differing petal sizes at each site. According to the plots, there are two groups containing identical shapes of petal patterns. The first group is the shape containing one pair of petals having the largest size, and the other two pairs of small petals having smaller and similar sizes [Figs. 3(b) and 3(d)]. When θ_r is parallel to a certain δ, the stronger tension

effectively pulls the Mo and S atoms, resulting in the larger ε_r. Simultaneously, the weaker circumferential tension at the middle of the remaining two δ directions results in the minor in-plane displacement of covalent bonds and the reduced ε_h. This allows the SHG polar plots to only possess one pair of the largest petals. The second group is where two pairs of larger petals shared similar sizes as indicated in Figs. 3(a), 3(c), and 3(e). This behavior arises from the stronger ε_r applied at the mid-point between atoms, when θ_r was equal to the average angle value of the other two δ. During the transition of ε_r applied closer to either the S or Mo atom, one of two pairs of large petals shrinks, but another pair expands, indicating the θ_r approaches the bigger petal's δ (Fig. S9). This is also demonstrated by the patterns in Fig. 2, where the orientation of ε_r was close to δ at 30°. Therefore, owing to the interaction between strain orientation and D_{3h} symmetry in monolayer TMD materials, the lattice undergoes periodic distortion and transformation, demonstrated by the same polar patterns with 60° rotation.

As in the section Results and Discussion, the multi-angular strain conditions of $\varepsilon_r = 2.19\%$, and $\varepsilon_h = 1.89\%$ [Figs. 3(f)–3(j)] could also be easily estimated [Eqs. (S2) and (S3) in supplementary material Note 1] and the r/R obtained by comparing the radius values of the bright fringe and the footprint radius of dome. Taking advantage of the strain conditions, Figs. 3(k)–3(o) present the corresponding analytical SHG polar patterns governed by Eq. (2), all of which have great agreement with the experimental patterns in terms of the pattern shape and rotation period. Some minor discrepancy could be attributed to the variation in strain magnitudes arisen from the ideal and actual dome geometries, as tiny side domes form around the boundary of the examined dome, which may deviate the actual shape from the circular round shape (Fig. S10).[34] Overall, the analytical solution confirms that with θ changing, the petal size and pattern shapes would periodically restore during this process, as the indication of the interaction between the mechanical tension and TMD lattice structure.

For a better visualization of the changes in the anisotropic SHG response for varying biaxial strain conditions, Fig. 4 presents a contour plot describing the evolution of the polar plots induced by strain orientations and the relative weight ratio of strain components. We measure the SH response of the atoms parallel to the horizontal axis (size of petal lying at 0°, P_0) and then monitor its changes when comparing it with the overall response values ($P_0 + P_{60} + P_{120}$) of atoms laying in three axes at 0°, 60°, and 120°, as indicated in Figs. 2, 3(a), and 3(k). The two extremes (0.042 and 0.72) of $P_0/(P_0 + P_{60} + P_{120})$ could be found when the strain ratio $\varepsilon_h/\varepsilon_r = 0$ and the principal $\theta_r = 90°$ and 0°, respectively. Accordingly, when the biaxial strain situation is close to that of uniaxial strain, it may result in greater lattice distortion as indicated by the increased slope and amplitude of the wave.[30,31] On the other hand, when the biaxial strain is nearly isotropic, the polar shape exhibits a uniform sixfold symmetry regardless of the strain orientation as seen by the flattening of the curve, which has great consistency and agreement with the experimental results.[50] Similar results were also found regarding the strain difference between biaxial components (Fig. S11). Therefore, this could be used as a quick tool to identify the existence of possible biaxial strain in different scenarios and to resolve its ratio and directions by applying polarization-dependent SHG measurement and observing one petal compared to others.
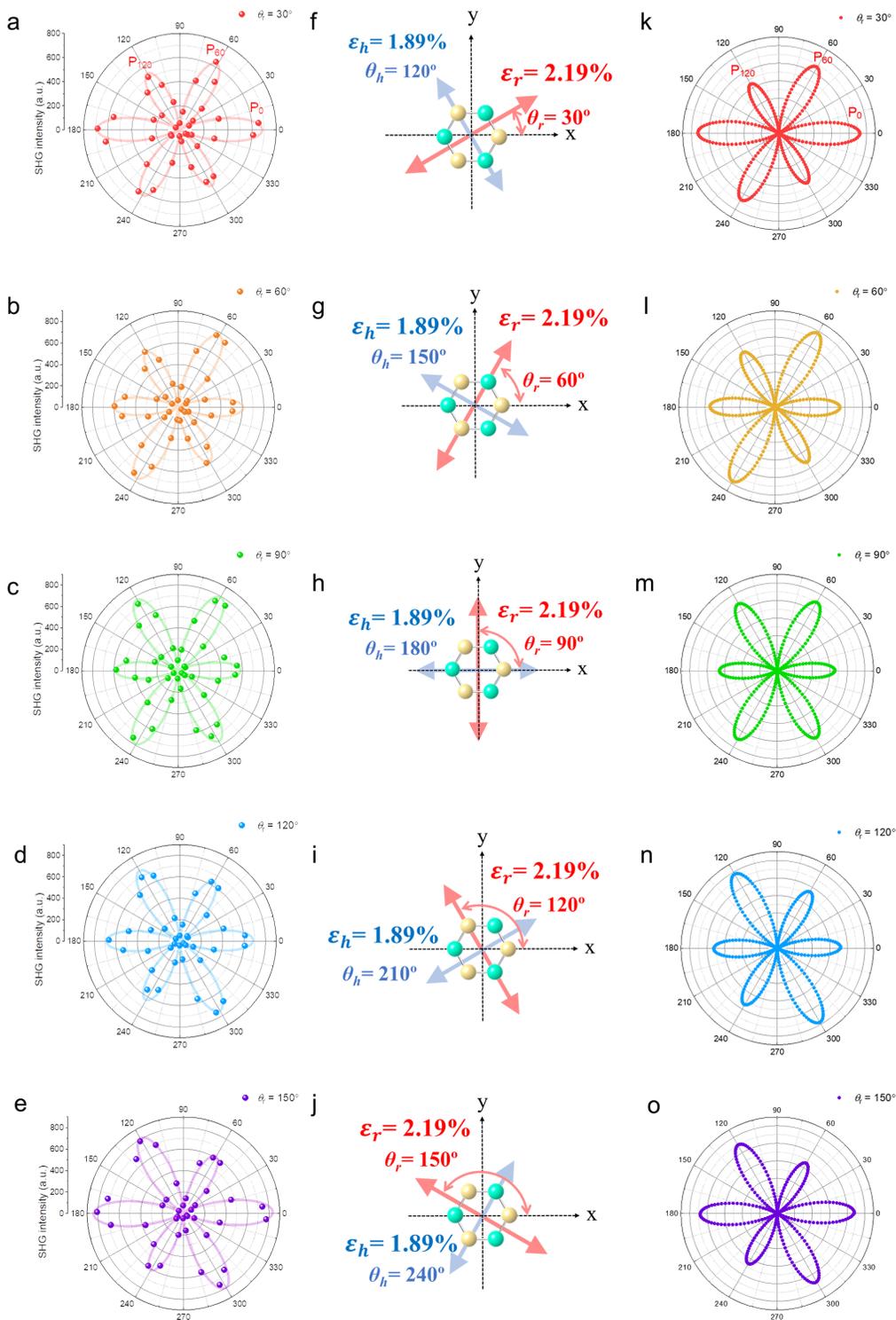
FIG. 3. Probing the anisotropic SH response with the evolution of the lattice distortion induced by varying biaxial strain orientations. (a)–(e) Experimental polarization-resolved SHG measured at the locations shown with different radial strain orientations but with the same magnitude. (f)–(j) Schematics of the strain conditions at the locations along a hoop of the dome, which are represented as arrows with the values of radial (ε_r, red arrow) and circumferential (ε_h, blue arrow) strains applied in various radial directions (30°–150°). (k-o) Analytical results of polarization-resolved SHG employed with the corresponding strain conditions in relation to the sites on the dome structure in (f)–(j).
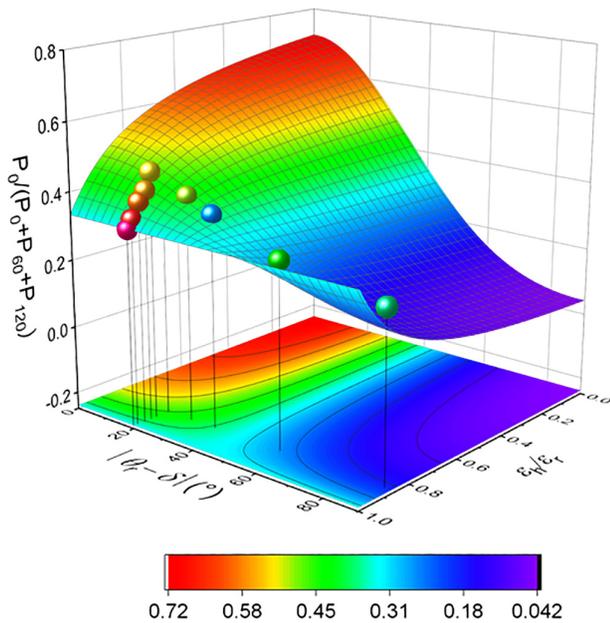
FIG. 4. Contour map showing the evolution of SHG polar pattern regarding strain ratio ($\varepsilon_h/\varepsilon_r$) and principal strain orientation ($\theta_r - \delta$). $P_0/(P_0 + P_{60} + P_{120})$ represents the variation in the sizes of petals located at 0°, 60°, and 120°. The values extracted from experimental SHG polar patterns are indicated by the spheres, and contour map is converted by the analytical patterns, both of which have great consistency under various strain conditions.

CONCLUSION

In conclusion, we have shown extraordinary SHG emission in TMD domes, exploiting this inherent feature to investigate the influence of biaxial strain vs the anisotropic SHG response. Owing to the distinct separation distance induced by the encapsulated pressurized hydrogen gas, TMD domes serve as the hemi-spherical optical resonator and possess internal in-phase interference, which can effectively achieve the enhanced light-matter interaction length and extraordinary increase in SHG emission. Therefore, the SHG magnitude enhancement is improved by 160 times in ambient condition and even remains robust in low temperature environments having at least 1 order of magnitude enhancement. It exhibits a promising approach to realize the effective enhancement in other nonlinear optical performance like third harmonic generation (THG) and four wave mixing (FWM). Moreover, polarization-dependent SHG was employed to comprehensively map anisotropic response induced by varying biaxial strain components over a diverging strain field in radial and circumferential directions. The results demonstrate that the anisotropic response of TMD films is less sensitive to the application of biaxial strain, as depicted by the less distorted polar plots, although the total magnitude of biaxial strain could be much larger than that of uniaxial strain. Our findings lay a strong foundation for the quick detection of possible anisotropic deformation in 2D materials and pave a promising path toward the realization of strain-engineered nonlinear optics with modest polarization selectivity for future quantum photonics and biomedical imaging and sensing devices.

Experimental methods

Sample fabrication

Thick TMD flakes were mechanically exfoliated onto SiO_2/Si (275 nm SiO_2), and then the samples were mounted in the vacuum chamber followed by low-energy proton irradiation in high vacuum condition. Meanwhile, within the ionization chamber, protons were produced and then accelerated by a grid system to produce an H^+ beam flushing the sample surface with low energies (between 5 and 20 eV). When target dose of protons was achieved, the treatment process completed and pressurized domes formed successfully, with the dose being determined by the treatment time and flux.

Optical characterizations

Optical microscopic images were taken by a Zeiss 780 confocal microscope equipped with 633 nm single photon laser. SHG measurements are performed on Zeiss 780 Confocal Microscopy. The fundamental laser field is provided tunable pulse laser Ti:Sapphire laser with a pulse width of 150 fs and a repetition rate of 80 MHz. The sample was excited and measured under a 50× confocal objective lens (NA = 0.85), and the results were collected in the reflection mode at a fundamental laser wavelength of 900 nm. During the measurements, the power of excitation light would be kept below 1 μW to avoid possible heating influence on the internal pressure and volume of the tested dome, ensuring the collected data with higher accuracy. An analyzer (polarizer) was used for polarization-resolved SHG to choose the SH radiation's polarization component, parallel to the polarization of the pump beam whose wavelength was set at 900 nm. The sample was placed on a rotational stage to collect the SH response in terms of polarization angles. Zeiss 780 confocal microscopy completes all tests and imaging for optical characterization measurements, where the high imaging resolution (pixel size = 0.03 μm) is used to capture more emission details of dome samples than the relatively low resolution (Fig. S12). All data were processed and analyzed by image processing software, Zen 3.4 (blue edition). Surface profiler (Veeco NT9100) employed with a 533 nm laser was used to obtain all the optical path length (OPL) values for dome samples in PSI mode.

Atomic force microscope measurement

The AFM measurements were captured using a Bruker Dimension Icon AFM. The topographic images, height profile, and the aspect ratio of the domes were obtained in Scanasyst air experiment mode with soft cantilevers, Scanasyst-Air, whose nominal spring constant k and nominal tip radius are 0.4 N/m and 2 nm, respectively.

SUPPLEMENTARY MATERIAL

See the supplementary material for details. All additional data and supplementary material regarding optical interference in dome, Raman results, and polarization-dependent SHG results are presented in the supplementary material file.

ACKNOWLEDGMENTS

AUTHOR DECLARATIONS
Conflict of Interest

The authors have no conflicts to disclose.

Author Contributions

Boqing Liu: Formal analysis (lead); Investigation (lead); Methodology (lead); Writing – original draft (lead). **Antonio Polimeni:** Supervision (equal); Writing – review & editing (equal). **Yuerui Lu:** Supervision (equal); Writing – review & editing (equal). **Tanju Yildirim:** Writing – original draft (supporting); Writing – review & editing (supporting). **Elena Blundo:** Investigation (supporting); Methodology (supporting); Writing – review & editing (supporting). **Domenico de Ceglia:** Investigation (supporting); Writing – review & editing (supporting). **Ahmed Raza Khan:** Investigation (supporting); Writing – review & editing (supporting). **Zongyou Yin:** Investigation (supporting); Supervision (supporting). **Hieu Nguyen:** Writing – review & editing (supporting). **Giorgio Pettinari:** Writing – review & editing (supporting). **Marco Felici:** Methodology (supporting).

DATA AVAILABILITY

The data that support the findings of this study are available from the corresponding authors upon reasonable request.

REFERENCES

[1] T. Helk, E. Berger, S. Jamnuch, L. Hoffmann, A. Kabacinski, J. Gautier, F. Tissandier, J.-P. Goddet, H.-T. Chang, J. Oh, C. D. Pemmaraju, T. A. Pascal, S. Sebban, C. Spielmann, and M. Zuerch, Sci. Adv. **7**(21), eabe2265 (2021).

[2] S. Shwartz, M. Fuchs, J. B. Hastings, Y. Inubushi, T. Ishikawa, T. Katayama, D. A. Reis, T. Sato, K. Tono, M. Yabashi, S. Yudovich, and S. E. Harris, Phys. Rev. Lett. **112**(16), 163901 (2014).

[3] T. Manaka, E. Lim, R. Tamura, and M. Iwamoto, Nat. Photonics **1**(10), 581–584 (2007).

[4] A. E. Willner, S. Khaleghi, M. R. Chitgarha, and O. F. Yilmaz, J. Lightwave Technol. **32**(4), 660–680 (2014).

[5] R. Trebino, K. W. DeLong, D. N. Fittinghoff, J. N. Sweetser, M. A. Krumbügel, B. A. Richman, and D. J. Kane, Rev. Sci. Instrum. **68**(9), 3277–3295 (1997).

[6] G. Wang, X. Marie, I. Gerber, T. Amand, D. Lagarde, L. Bouet, M. Vidal, A. Balocchi, and B. Urbaszek, Phys. Rev. Lett. **114**(9), 097403 (2015).

[7] Z. Ye, T. Cao, K. O'Brien, H. Zhu, X. Yin, Y. Wang, S. G. Louie, and X. Zhang, Nature **513**(7517), 214–218 (2014).

[8] W.-T. Hsu, Z.-A. Zhao, L.-J. Li, C.-H. Chen, M.-H. Chiu, P.-S. Chang, Y.-C. Chou, and W.-H. Chang, ACS Nano **8**(3), 2951–2958 (2014).

[9] C. Jin, E. C. Regan, A. Yan, M. Iqbal Bakti Utama, D. Wang, S. Zhao, Y. Qin, S. Yang, Z. Zheng, S. Shi, K. Watanabe, T. Taniguchi, S. Tongay, A. Zettl, and F. Wang, Nature **567**(7746), 76–80 (2019).

[10] J. Y. Chauleau, E. Haltz, C. Carrétéro, S. Fusil, and M. Viret, Nat. Mater. **16**(8), 803–807 (2017).

[11] K.-Q. Lin, S. Bange, and J. M. Lupton, Nat. Phys. **15**(3), 242–246 (2019).

[12] Y. Wang, J. Xiao, S. Yang, Y. Wang, and X. Zhang, Opt. Mater. Express **9**(3), 1136–1149 (2019).

[13] W. Wu, L. Wang, Y. Li, F. Zhang, L. Lin, S. Niu, D. Chenet, X. Zhang, Y. Hao, T. F. Heinz, J. Hone, and Z. L. Wang, Nature **514**(7523), 470–474 (2014).

[14] L. M. Malard, T. V. Alencar, A. P. M. Barboza, K. F. Mak, and A. M. de Paula, Phys. Rev. B **87**(20), 201401 (2013).

[15] N. Kumar, S. Najmaei, Q. Cui, F. Ceballos, P. M. Ajayan, J. Lou, and H. Zhao, Phys. Rev. B **87**(16), 161403 (2013).

[16] A. Castellanos-Gomez, R. Roldán, E. Cappelluti, M. Buscema, F. Guinea, H. S. J. van der Zant, and G. A. Steele, Nano Lett. **13**(11), 5361–5366 (2013).

[17] S. Bertolazzi, J. Brivio, and A. Kis, ACS Nano **5**(12), 9703–9709 (2011).

[18] A. Falin, M. Holwill, H. Lv, W. Gan, J. Cheng, R. Zhang, D. Qian, M. R. Barnett, E. J. G. Santos, K. S. Novoselov, T. Tao, X. Wu, and L. H. Li, ACS Nano **15**(2), 2600–2610 (2021).

[19] E. Blundo, C. Di Giorgio, G. Pettinari, T. Yildirim, M. Felici, Y. Lu, F. Bobba, and A. Polimeni, Adv. Mater. Interfaces **7**(17), 2000621 (2020).

[20] T. K. Fryett, K. L. Seyler, J. Zheng, C.-H. Liu, X. Xu, and A. Majumdar, 2D Mater. **4**(1), 015031 (2016).

[21] R. Trivedi, U. K. Khankhoje, and A. Majumdar, Phys. Rev. Appl. **5**(5), 054001 (2016).

[22] A. R. Khan, L. Zhang, K. Ishfaq, A. Ikram, T. Yildirim, B. Liu, S. Rahman, and Y. Lu, Adv. Funct. Mater. **32**(3), 2105259 (2021).

[23] K. L. Seyler, J. R. Schaibley, P. Gong, P. Rivera, A. M. Jones, S. Wu, J. Yan, D. G. Mandrus, W. Yao, and X. Xu, Nat. Nanotechnol. **10**(5), 407–411 (2015).

[24] E. Blundo, E. Cappelluti, M. Felici, G. Pettinari, and A. Polimeni, Appl. Phys. Rev. **8**(2), 021318 (2021).

[25] K. He, C. Poole, K. F. Mak, and J. Shan, Nano Lett. **13**(6), 2931–2936 (2013).

[26] H. J. Conley, B. Wang, J. I. Ziegler, R. F. Haglund, S. T. Pantelides, and K. I. Bolotin, Nano Lett. **13**(8), 3626–3630 (2013).

[27] T. T. Tran, K. Bray, M. J. Ford, M. Toth, and I. Aharonovich, Nat. Nanotechnol. **11**(1), 37–41 (2016).

[28] H. Moon, G. Grosso, C. Chakraborty, C. Peng, T. Taniguchi, K. Watanabe, and D. Englund, Nano Lett. **20**(9), 6791–6797 (2020).

[29] L. Mennel, V. Smejkal, L. Linhart, J. Burgdörfer, F. Libisch, and T. Mueller, Nano Lett. **20**(6), 4242–4248 (2020).

[30] J. Liang, J. Zhang, Z. Li, H. Hong, J. Wang, Z. Zhang, X. Zhou, R. Qiao, J. Xu, P. Gao, Z. Liu, Z. Liu, Z. Sun, S. Meng, K. Liu, and D. Yu, Nano Lett. **17**(12), 7539–7543 (2017).

[31] A. R. Khan, B. Liu, T. Lu, L. Zhang, A. Sharma, Y. Zhu, W. Ma, and Y. Lu, ACS Nano **14**(11), 15806–15815 (2020).

[32] E. Blundo, T. Yildirim, G. Pettinari, and A. Polimeni, Phys. Rev. Lett. **127**(4), 046101 (2021).

[33] L. Mennel, M. M. Furchi, S. Wachter, M. Paur, D. K. Polyushkin, and T. Mueller, Nat. Commun. **9**(1), 516 (2018).

[34] D. Tedeschi, E. Blundo, M. Felici, G. Pettinari, B. Liu, T. Yildirim, E. Petroni, C. Zhang, Y. Zhu, and S. Sennato, Adv. Mater. **31**(44), 1903795 (2019).

[35] Z. Dai, Y. Hou, D. A. Sanchez, G. Wang, C. J. Brennan, Z. Zhang, L. Liu, and N. Lu, Phys. Rev. Lett. **121**(26), 266101 (2018).

[36] D. Lloyd, X. Liu, N. Boddeti, L. Cantley, R. Long, M. L. Dunn, and J. S. Bunch, Nano Lett. **17**(9), 5329–5334 (2017).

[37] E. Khestanova, F. Guinea, L. Fumagalli, A. K. Geim, and I. V. Grigorieva, Nat. Commun. **7**, 12587 (2016).

[38] B. Liu, T. Yildirim, T. Lü, E. Blundo, L. Wang, L. Jiang, H. Zou, L. Zhang, H. Zhao, Z. Yin, F. Tian, A. Polimeni, and Y. Lu, Nat. Commun. **14**(1), 1050 (2023).

[39] E. Blundo, M. Felici, T. Yildirim, G. Pettinari, D. Tedeschi, A. Miriametro, B. Liu, W. Ma, Y. Lu, and A. Polimeni, Phys. Rev. Res. **2**(1), 012024 (2020).

[40] T. P. Darlington, C. Carmesin, M. Florian, E. Yanev, O. Ajayi, J. Ardelean, D. A. Rhodes, A. Ghiotto, A. Krayev, K. Watanabe, T. Taniguchi, J. W. Kysar, A. N. Pasupathy, J. C. Hone, F. Jahnke, N. J. Borys, and P. J. Schuck, Nat. Nanotechnol. **15**(10), 854–860 (2020).

[41] K. Beach, M. C. Lucking, and H. Terrones, Phys. Rev. B **101**(15), 155431 (2020).

[42] A. R. Khan, B. Liu, L. Zhang, Y. Zhu, X. He, L. Zhang, T. Lü, and Y. Lu, Adv. Opt. Mater. **8**(17), 2000441 (2020).

[43] A. Ciattoni, A. Marini, C. Rizza, and C. Conti, Light **7**(1), 5 (2018).

[44] A. Pramanik, S. R. Chavva, Z. Fan, S. S. Sinha, B. P. Nellore, and P. C. Ray, J. Phys. Chem. Lett. **5**(12), 2150–2154 (2014).

08 June 2025 23:52:08

[45]J. L. Li, H. C. Bao, X. L. Hou, L. Sun, X. G. Wang, and M. Gu, Angew. Chem., Int. Ed. **51**(8), 1830–1834 (2012).

[46]H. Dong, S. Tang, Y. Hao, H. Yu, W. Dai, G. Zhao, Y. Cao, H. Lu, X. Zhang, and H. Ju, ACS Appl. Mater. Interfaces **8**(5), 3107–3114 (2016).

[47]I. L. Lyubchanskii, N. N. Dadoenkova, M. I. Lyubchanskii, T. Rasing, J.-W. Jeong, and S.-C. Shin, Appl. Phys. Lett. **76**(14), 1848–1850 (2000).

[48]S. P. Koenig, N. G. Boddeti, M. L. Dunn, and J. S. Bunch, Nat. Nanotechnol. **6**, 543 (2011).

[49]Y. Li, Y. Rao, K. F. Mak, Y. You, S. Wang, C. R. Dean, and T. F. Heinz, Nano Lett. **13**(7), 3329–3333 (2013).

[50]L. Mennel, M. Paur, and T. Mueller, APL Photonics **4**(3), 034404 (2019).

08 June 2025 23:52:08